Biomedical Optics EXPRESS

# Phantom and mouse experiments of time-domain fluorescence tomography using total light approach

**Shinpei Okawa,[1,2,*] Akira Yano,[3] Kazuki Uchida,[3] Yohei Mitsui,[3] Masaki Yoshida,[3] Masashi Takekoshi,[3] Andhi Marjono,[3] Feng Gao,[4] Yoko Hoshi,[5] Ikuhiro Kida,[5] Kazuto Masamoto,[6] and Yukio Yamada[1]**

[1]*Department of Mechanical Engineering and Intelligent Systems, University of Electro-Communications, 1-5-1 Chofuga-oka, Chofu, Tokyo 182-8585, Japan*
[2]*Currently with the Department of Medical Engineering, National Defense Medical College, 3-2 Namiki, Tokorozawa, Saitama 359-8513, Japan*
[3]*Graduate students of the Department of Mechanical Engineering and Intelligent Systems, University of Electro-Communications, 1-5-1 Chofuga-oka, Chofu, Tokyo 182-8585, Japan*
[4]*College of Precision Instrument and Optoelectronics Engineering, Tianjin University, Tianjin 300072, China*
[5]*Integrated Neuroscience Research Project, Tokyo Metropolitan Institute of Medical Science, 2-1-6 Kami-kitazawa, Setagaya, Tokyo 156-8506, Japan*
[6]*Center for Frontier Science and Engineering, University of Electro-Communications, 1-5-1 Chofuga-oka, Chofu, Tokyo 182-8585, Japan*
**okawa@ndmc.ac.jp*

**Abstract:** Phantom and mouse experiments of time-domain fluorescence tomography were conducted to demonstrate the total light approach which was previously proposed by authors. The total light approach reduces the computation time to solve the forward model for light propagation. Time-resolved temporal profiles were acquired for cylindrical phantoms having single or double targets containing indocyanine green (ICG) solutions. The reconstructed images of ICG concentration reflected the true distributions of ICG concentration with a spatial resolution of about 10 mm. *In vivo* experiments were conducted using a mouse in which an ICG capsule was embedded beneath the skin in the abdomen. The reconstructed image of the ICG concentration again reflected the true distribution of ICG although artifacts due to autofluorescence appeared in the vicinity of the skin. The effectiveness of the total light approach was demonstrated by the phantom and mouse experiments.



**OCIS codes:** (170.3880) Medical and biological imaging; (170.6280) Spectroscopy, fluorescence and luminescence.

## References and links

1. T. F. Massoud and S. S. Gambhir, "Molecular imaging in living subjects: seeing fundamental biological processes in a new light," Genes Dev. **17**(5), 545–580 (2003).
2. S. R. Cherry, "*In vivo* molecular and genomic imaging: new challenges for imaging physics," Phys. Med. Biol. **49**(3), R13–R48 (2004).
3. V. Ntziachristos, C. H. Tung, C. Bremer, and R. Weissleder, "Fluorescence molecular tomography resolves protease activity *in vivo*," Nat. Med. **8**(7), 757–761 (2002).
4. V. Ntziachristos and R. Weissleder, "Experimental three-dimensional fluorescence reconstruction of diffuse media by use of a normalized Born approximation," Opt. Lett. **26**(12), 893–895 (2001).
5. S. R. Arridge, "Optical tomography in medical imaging," Inverse Probl. **15**(2), R41–R93 (1999).
6. Y. Yamada, "Light-tissue interaction and optical imaging in biomedicine," in *Annual Review of Heat Transfer*, C.-L. Tien, ed. (Begell House, 1995), Vol. 6, pp. 1–59.
7. F. Gao, H. Zhao, and Y. Yamada, "Improvement of image quality in diffuse optical tomography by use of full time-resolved data," Appl. Opt. **41**(4), 778–791 (2002).
8. X. Zhang, C. T. Badea, and G. A. Johnson, "Three-dimensional reconstruction in free-space whole-body fluorescence tomography of mice using optically reconstructed surface and atlas anatomy," J. Biomed. Opt. **14**(6), 064010 (2009).
9. N. Deliolanis, T. Lasser, D. Hyde, A. Soubret, J. Ripoll, and V. Ntziachristos, "Free-space fluorescence molecular tomography utilizing 360° geometry projections," Opt. Lett. **32**(4), 382–384 (2007).

#178955 - $15.00 USD Received 31 Oct 2012; revised 12 Jan 2013; accepted 14 Feb 2013; published 28 Mar 2013

10. M. Solomon, B. R. White, R. E. Nothdruft, W. Akers, G. Sudlow, A. T. Eggebrecht, S. Achilefu, and J. P. Culver, "Video-rate fluorescence diffuse optical tomography for *in vivo* sentinel lymph node imaging," Biomed. Opt. Express **2**(12), 3267–3277 (2011).
11. M. S. Patterson and B. W. Pogue, "Mathematical model for time-resolved and frequency-domain fluorescence spectroscopy in biological tissues," Appl. Opt. **33**(10), 1963–1974 (1994).
12. D. Y. Paithankar, A. U. Chen, B. W. Pogue, M. S. Patterson, and E. M. Sevick-Muraca, "Imaging of fluorescent yield and lifetime from multiply scattered light reemitted from random media," Appl. Opt. **36**(10), 2260–2272 (1997).
13. M. Freiberger, C. Clason, and H. Scharfetter, "Adaptation and focusing of optode configurations for fluorescence optical tomography by experimental design methods," J. Biomed. Opt. **15**(1), 016024 (2010).
14. A. B. Milstein, S. Oh, K. J. Webb, C. A. Bouman, Q. Zhang, D. A. Boas, and R. P. Millane, "Fluorescence optical diffusion tomography," Appl. Opt. **42**(16), 3081–3094 (2003).
15. S. C. Davis, H. Dehghani, J. Wang, S. Jiang, B. W. Pogue, and K. D. Paulsen, "Image-guided diffuse optical fluorescence tomography implemented with Laplacian-type regularization," Opt. Express **15**(7), 4066–4082 (2007).
16. S. C. Davis, B. W. Pogue, R. Springett, C. Leussler, P. Mazurkewitz, S. B. Tuttle, S. L. Gibbs-Strauss, S. S. Jiang, H. Dehghani, and K. D. Paulsen, "Magnetic resonance-coupled fluorescence tomography scanner for molecular imaging of tissue," Rev. Sci. Instrum. **79**(6), 064302 (2008).
17. H. Dehghani, M. E. Eames, P. K. Yalavarthy, S. C. Davis, S. Srinivasan, C. M. Carpenter, B. W. Pogue, and K. D. Paulsen, "Near infrared optical tomography using NIRFAST: Algorithm for numerical model and image reconstruction," Commun. Numer. Methods Eng. **25**(6), 711–732 (2009).
18. S. Lam, F. Lesage, and X. Intes, "Time Domain Fluorescent Diffuse Optical Tomography: analytical expressions," Opt. Express **13**(7), 2263–2275 (2005).
19. F. Gao, H. Zhao, Y. Tanikawa, and Y. Yamada, "A linear, featured-data scheme for image reconstruction in time-domain fluorescence molecular tomography," Opt. Express **14**(16), 7109–7124 (2006).
20. F. Gao, H. Zhao, L. Zhang, Y. Tanikawa, A. Marjono, and Y. Yamada, "A self-normalized, full time-resolved method for fluorescence diffuse optical tomography," Opt. Express **16**(17), 13104–13121 (2008).
21. A. Marjono, A. Yano, S. Okawa, F. Gao, and Y. Yamada, "Total light approach of time-domain fluorescence diffuse optical tomography," Opt. Express **16**(19), 15268–15285 (2008).
22. M. J. Niedre, R. H. de Kleine, E. Aikawa, D. G. Kirsch, R. Weissleder, and V. Ntziachristos, "Early photon tomography allows fluorescence detection of lung carcinomas and disease progression in mice in vivo," Proc. Natl. Acad. Sci. U.S.A. **105**(49), 19126–19131 (2008).
23. R. E. Nothdurft, S. V. Patwardhan, W. Akers, Y. Ye, S. Achilefu, and J. P. Culver, "In vivo fluorescence lifetime tomography," J. Biomed. Opt. **14**(2), 024004 (2009).
24. D. S. Kepshire, S. L. Gibbs-Strauss, J. A. O'Hara, M. Hutchins, N. Mincu, F. Leblond, M. Khayat, H. Dehghani, S. Srinivasan, and B. W. Pogue, "Imaging of glioma tumor with endogenous fluorescence tomography," J. Biomed. Opt. **14**(3), 030501 (2009).
25. F. Gao, J. Li, L. Zhang, P. Poulet, H. Zhao, and Y. Yamada, "Simultaneous fluorescence yield and lifetime tomography from time-resolved transmittances of small-animal-sized phantom," Appl. Opt. **49**(16), 3163–3172 (2010).
26. A. D. Klose and A. H. Hielscher, "Fluorescence tomography with simulated data based on the equation of radiative transfer," Opt. Lett. **28**(12), 1019–1021 (2003).
27. A. D. Klose, V. Ntziachristos, and A. H. Hielscher, "The inverse source problem based on the radiative transfer equation in optical molecular imaging," J. Comput. Phys. **202**(1), 323–345 (2005).
28. F. Gao, A. Marjono, S. Okawa, and Y. Yamada, "Light Propagation for Time-Domain Fluorescence Diffuse Optical Tomography by Convolution Using Lifetime Function," Opt. Rev. **14**(3), 131–138 (2007).
29. K. Furutsu and Y. Yamada, "Diffusion approximation for a dissipative random medium and the applications," Phys. Rev. E Stat. Phys. Plasmas Fluids Relat. Interdiscip. Topics **50**(5), 3634–3640 (1994).
30. M. Schweiger, S. R. Arridge, and D. T. Delpy, "Application of the Finite-Element Method for the Forward and Inverse Models in Optical Tomography," J. Math. Imaging Vis. **3**(3), 263–283 (1993).
31. W. H. Press, B. P. Flannery, S. A. Teukolsky, and W. T. Vetterling, in *Numerical Recipes in C* (Cambridge University Press, 1988).
32. B. Yuan, N.-G. Chen, and Q. Zhu, "Emission and absorption properties of indocyanine green in Intralipid solution," J. Biomed. Opt. **9**(3), 497–503 (2004).
33. E. M. Sevik-Muraca, A. Godavarthy, J. P. Houston, A. B. Thompson, and R. Roy, "Near-Infrared Imaging with Fluorescent Contrast Agents," in *Handbook of Biomedical Fluorescence*, M.-A. Mycek and B. W. Pogue, eds. (Marcel Dekker, 2003), Chap. 14, pp. 475–476.
34. M. Y. Berezin, H. Lee, W. Akers, and S. Achilefu, "Near infrared dyes as lifetime solvatochromic probes for micropolarity measurements of biological systems," Biophys. J. **93**(8), 2892–2899 (2007).
35. H. Eda, I. Oda, Y. Ito, Y. Wada, Y. Oikawa, Y. Tsunazawa, M. Takada, Y. Tsuchiya, Y. Yamashita, M. Oda, A. Sassaroli, Y. Yamada, and M. Tamura, "Multichannel time-resolved optical tomographic imaging system," Rev. Sci. Instrum. **70**(9), 3595–3602 (1999).
36. E. M. C. Hillman, J. C. Hebden, F. E. W. Schmidt, S. R. Arridge, M. Schweiger, H. Dehghani, and D. T. Delpy, "Calibration techniques and datatype extraction for time-resolved optical tomography," Rev. Sci. Instrum. **71**(9), 3415–3427 (2000).
37. S. Okawa, Y. Hoshi, and Y. Yamada, "Improvement of image quality of time-domain diffuse optical tomography with $l_p$ sparsity regularization," Biomed. Opt. Express **2**(12), 3334–3348 (2011).

#178955 - $15.00 USD Received 31 Oct 2012; revised 12 Jan 2013; accepted 14 Feb 2013; published 28 Mar 2013

38. T. Shimokawa, T. Kosaka, O. Yamashita, N. Hiroe, T. Amita, Y. Inoue, and M. A. Sato, "Hierarchical Bayesian estimation improves depth accuracy and spatial resolution of diffuse optical tomography," Opt. Express **20**(18), 20427–20446 (2012).
39. F. Leblond, S. C. Davis, P. A. Valdés, and B. W. Pogue, "Pre-clinical whole-body fluorescence imaging: Review of instruments, methods and applications," J. Photochem. Photobiol. B **98**(1), 77–94 (2010).

## 1. Introduction

Over the last decade, a large number of research and development has conducted for the technology of molecular imaging, and one of the modalities of molecular imaging is fluorescence diffuse optical tomography (FDOT) [1,2]. FDOT is an emerging technology to image spatial distributions of fluorescence parameters in tissues which are irradiated by a near-infrared (NIR) excitation light source and emit fluorescence light [3,4]. The fluorescence parameters include fluorophore concentration, fluorescence quantum yield and lifetime. Accumulation into and secretion from specified organs of the target drug labeled with a fluorophore can be investigated by tracing the temporal change of the fluorophore concentration. Fluorescence quantum yield and lifetime can give information about the tissue microenvironments such as temperature, viscosity, pH, etc. on which they are dependent.

Essentially, FDOT is an extension of the technology of diffuse optical tomography (DOT) [5,6]. DOT reconstructs the tomographic images of absorption and scattering characteristics inside the tissue from the data of detected light intensities which are irradiated onto and reemitted from the tissue surface using the reconstruction algorithm based on the inversion technique. Usually, near-infrared light is used due to its high transmission capability through biological tissues, and the images of absorption characteristics are converted to the images of physiological information through the absorption spectra of chromophores in biological tissues, such as hemoglobin and myoglobin. The technique of DOT can be classified into three modes according to the type of source light, (i) continuous wave (CW), (ii) frequency domain and (iii) time domain. Because the number of useful data for reconstruction increases in this order, time domain mode is believed to give the images with highest quality with the costs of sophisticated instruments for measurement and long computation times for reconstruction [7].

These three modes can be used for FDOT as well. So far, CW and frequency domain modes have been mainly used for FDOT and many results have been reported [8–17] because time domain mode needs complicated and expensive instruments and takes longer time to acquire data for reconstruction. However, it is difficult for CW mode [8–10] to measure the fluorescence lifetime which has the order of nanosecond. Frequency and time domain modes can reconstruct both the fluorescence concentration and lifetime, but so far many FDOT investigations have been conducted using frequency domain mode [11–17] while those using time domain mode are limited. FDOT investigations using time domain mode have been conducted by simulations [18–21] first, and some experimental works have been reported recently [22–25].

In reconstruction for FDOT, the forward model of light propagation is based on the photon diffusion equations for excitation and emission light. Particularly for time domain mode, the emission source term in the photon diffusion equation for emission light is a convolution integral of the excitation light fluence and the fluorescence lifetime function. This integral makes the computation of the forward model complex and long. To avoid the computation of the convolution integral, the total light approach was proposed previously and simulation results were presented [21].

The purpose of this study is to experimentally demonstrate the total light approach for time domain FDOT [21] by showing the experimental results using phantoms and mouse. Time-resolved measurement employing a time correlated single photon counting system requires longer time for data acquisition with a satisfactory S/N ratio than CW or frequency domain modes. But it has been reported that high quality images of DOT can be reconstructed with the use of the time-resolved data at the costs of long computation and large memory [7], and time domain FDOT can provide the images of the fluorescence characteristics such as the fluorophore concentrations, the fluorescence quantum yield and lifetime [20,25]. In the

#178955 - $15.00 USD Received 31 Oct 2012; revised 12 Jan 2013; accepted 14 Feb 2013; published 28 Mar 2013

previously proposed total light approach, however, the fluorescence quantum yield and lifetime are assumed to be known and only the fluorophore concentrations were reconstructed. Therefore, the total light approach does not fully utilize the advantages of time domain mode. But the previous report of FDOT simulations employing the total light approach easily reconstructed the fluorophore concentration with the measured mean time-of-flight data as the featured input data for reconstruction. To our knowledge, none of the reported experimental investigations using time-resolved measurement [22–25] has used the mean time-of-flight data obtained from the measured time-resolved profiles. Niedre et al. [22] used the early photons in the time period of 100 ps for reconstruction, Northdurft et al. [23] and Kepshire et al. [24] converted the measured time domain data to frequency domain data for reconstruction, and Gao et al. [25] employed the generalized pulse spectrum technique for reconstruction where the measured time-resolved data were Laplace transformed. As the first step toward the full use of the time-resolved measurement data for FDOT, this study reports the experimental results of time domain FDOT to demonstrate the total light approach using the measured mean time-of-flight data as the featured input data.

In the demonstration experiments in this study, we focus our attention only on imaging the fluorophore concentrations within the objects of cylindrical phantoms and a mouse *in vivo*. Indocyanine green (ICG) was used as a fluorophore, and capsules containing ICG were inserted inside the phantoms and mouse abdomen. The data were acquired with a time-resolved measurement technique, and the tomographic images of ICG concentrations in the capsules were reconstructed by use of the total light approach. In the following, the total light approach is briefly explained, the experimental method including the instruments and objects are described, the experimental results are reported, and finally the conclusions are stated.

## 2. Image reconstruction using the total light approach

### *2.1 Formulation of the forward problem by total light*

Image reconstruction is performed by solving the inverse problem where the forward problem for propagation of fluorescence excitation and emission light must be modeled. Light propagation in random media is strictly described by the radiative transfer equation (RTE), and some investigations of FDOT based on RTE have been reported [26,27] but limited to CW mode probably due to the heavy computational load. Then, the photon diffusion equation which is the diffusion approximation of RTE is frequently used for the model of light propagation in biological objects with diameters larger than 10 mm [5,6]. The time dependent photon diffusion equations for excitation and emission light are expressed by Eqs. (1) and (2) [11,28].

$$\left[-\nabla\cdot(D(\mathbf{r})\nabla)+\mu_a(\mathbf{r})+\varepsilon N(\mathbf{r})+\frac{1}{c}\frac{\partial}{\partial t}\right]\Phi_x(\mathbf{r},t)=q_x(\mathbf{r},t), \tag{1}$$

$$\left[-\nabla\cdot(D(\mathbf{r})\nabla)+\mu_a(\mathbf{r})+\frac{1}{c}\frac{\partial}{\partial t}\right]\Phi_m(\mathbf{r},t)=\gamma\varepsilon N(\mathbf{r})\int_0^\infty\Phi_x(\mathbf{r},t')\cdot\frac{1}{\tau}\exp\{-(t-t')/\tau\}dt', \tag{2}$$

where $\mathbf{r}$ [mm] is the position vector, $t$ [ps] the time, $\Phi(\mathbf{r},t)$ [W/mm$^2$] the fluence rate, $q(\mathbf{r},t)$ [W/mm$^3$] the internal light source, $c$ [mm/ps] the speed of light in the object, $D(\mathbf{r})$ [mm] the photon diffusion coefficient, $\mu_a(\mathbf{r})$ [mm$^{-1}$] the absorption coefficient, $\varepsilon$ [mm$^{-1}$μM$^{-1}$] the specific extinction coefficient of the fluorophore for the excitation light, $N(\mathbf{r})$ [μM] the concentration of the fluorophore, $\tau$ [ns] the lifetime of the fluorophore, $\gamma$ the quantum yield of the fluorophore, subscripts $x$ and $m$ denote the excitation and emission light. The photon diffusion coefficient is expressed as $D(\mathbf{r}) = 1/(3\mu_s'(\mathbf{r}))$ using the reduced scattering coefficient, $\mu_s'(\mathbf{r})$ [29]. Because the wavelength of excitation is different from that of emission $D(\mathbf{r})$ and $\mu_a(\mathbf{r})$ in Eq. (1) are different from those in Eq. (2). But the difference in the wavelength is as small as about 10 nm, $D(\mathbf{r})$ and $\mu_a(\mathbf{r})$ for excitation wavelength are assumed equal to those for

#178955 - $15.00 USD Received 31 Oct 2012; revised 12 Jan 2013; accepted 14 Feb 2013; published 28 Mar 2013

emission wavelength. Also, the specific extinction coefficient, $\varepsilon$, and the quantum yield, $\gamma$, are assumed to be known and homogeneous within the object.

The right hand side of Eq. (2) is the emission term which is the convolution of the fluence rate of excitation light, $\Phi_x(\mathbf{r},t)$, and the lifetime function, $\exp(-t/\tau)/\tau$, and needs long computation time. Now the total light approach is introduced as follows [21]. Assuming an ideal fluorescence with infinitesimal lifetime, i.e. $\tau = 0$, modifies Eq. (2) as Eq. (3),

$$\left[-\nabla\cdot(D(\mathbf{r})\nabla)+\mu_a(\mathbf{r})+\frac{1}{c}\frac{\partial}{\partial t}\right]\Phi_m^*(\mathbf{r},t)=\gamma\varepsilon N(\mathbf{r})\Phi_x(\mathbf{r},t'), \tag{3}$$

where $\Phi^*_m(\mathbf{r},t)$ is the fluence rate of emission when $\tau = 0$, namely the zero-lifetime emission, and is related to the real fluence rate of emission, $\Phi_m(\mathbf{r},t)$, as Eq. (4),

$$\Phi_m(\mathbf{r},t)=\int_0^\infty \Phi_m^*(\mathbf{r},t')\cdot\frac{1}{\tau}\exp\{-(t-t')/\tau\}dt'. \tag{4}$$

Now we define the total light $\Phi_T(\mathbf{r},t)$ as the following Eq. (5),

$$\Phi_T(\mathbf{r},t)=\Phi_x(\mathbf{r},t)+\frac{1}{\gamma}\Phi_m^*(\mathbf{r},t). \tag{5}$$

Then the photon diffusion equation for the total light, $\Phi_T(\mathbf{r},t)$, is derived from Eqs. (1) and (3) as the following,

$$\left[-\nabla\cdot(D(\mathbf{r})\nabla)+\mu_a(\mathbf{r})+\frac{1}{c}\frac{\partial}{\partial t}\right]\Phi_T(\mathbf{r},t)=q_x(\mathbf{r},t). \tag{6}$$

Physically, the total light is understood as the sum of excitation and emission light under the extreme fluorescence condition where all the absorbed energy of excitation light is converted to fluorescence light ($\gamma = 1$) with the zero-lifetime ($\tau = 0$). Introducing the total light converts the combined fundamental equations from Eqs. (1) and (2) to Eqs. (1) and (6). The difference between Eqs. (1) and (6) is only the term of absorption of excitation light, $\varepsilon N(\mathbf{r})$, and thus the solutions of $\Phi_x(\mathbf{r},t)$ and $\Phi_T(\mathbf{r},t)$ from Eqs. (1) and (6) are numerically obtained more easily and faster than the solutions of $\Phi_x(\mathbf{r},t)$ and $\Phi_m(\mathbf{r},t)$ from Eqs. (1) and (2) using the finite element method (FEM) [30]. The fluorophore concentration, $N(\mathbf{r})$, is obtained by reconstructing $\mu_a(\mathbf{r}) + \varepsilon N(\mathbf{r})$ in Eq. (1) and $\mu_a(\mathbf{r})$ in Eq. (6) first, then by dividing the subtraction $\{[\mu_a(\mathbf{r}) + \varepsilon N(\mathbf{r})] - \mu_a(\mathbf{r})\}$ by $\varepsilon$.

The boundary conditions for Eqs. (1), (2) and (6) are given as the following,

$$-D(\mathbf{r}_b)\nabla_n\Phi_v(\mathbf{r}_b,t)=\frac{1}{2A}\Phi_v(\mathbf{r}_b,t),\quad (v=x,m,T), \tag{7}$$

where $\mathbf{r}_b$ is the position at the boundary, $\nabla_n$ the gradient outward normal to the boundary, $A=(1+R_f)/(1-R_f)$ the factor with the internal reflectivity at the boundary, $R_f$, and the subscript $v$ represents $x$, $m$, or $T$. $R_f$ is given by Eq. (8),

$$R_f=-1.440n^{-2}+0.710n^{-1}+0.668+0.0636n, \tag{8}$$

where $n$ is the ratio of the refractive index of the object to that of the environment.

The initial condition is given by Eq. (9),

$$\Phi_v(\mathbf{r},t)=0 \ \text{ for } t\le 0,\quad (v=x,m,T). \tag{9}$$

$\Phi_x(\mathbf{r},t)$ and $\Phi_T(\mathbf{r},t)$ are calculated from Eqs. (1) and (6) under the boundary and initial conditions (7) and (9). Then $\Phi_m(\mathbf{r},t)$ is calculated from Eqs. (5) and (4) as the solution of the forward problem.

#178955 - $15.00 USD Received 31 Oct 2012; revised 12 Jan 2013; accepted 14 Feb 2013; published 28 Mar 2013

The measured powers of the excitation, fluorescence and total light, $\Gamma_x(\mathbf{r}_b,t)$, $\Gamma_m(\mathbf{r}_b,t)$, $\Gamma_T(\mathbf{r}_b,t)$, are the fluxes of the fluence rates of the excitation, fluorescence and total light, $\Phi_x(\mathbf{r},t)$, $\Phi_m(\mathbf{r},t)$ and $\Phi_T(\mathbf{r},t)$, at the boundary as expressed by Eq. (10),

$$\Gamma_\nu(\mathbf{r}_b,t) = -D(\mathbf{r}_b)\nabla_n \Phi_\nu(\mathbf{r}_b,t), \quad (\nu = x,m,T). \tag{10}$$

From Eq. (7), the measured powers, $\Gamma_\nu(\mathbf{r}_b,t)$, become proportional to the fluence rates, $\Phi_\nu(\mathbf{r},t)$, as shown in Eq. (11),

$$\Gamma_\nu(\mathbf{r}_b,t) = \frac{1}{2A}\Phi_\nu(\mathbf{r}_b,t), \quad (\nu = x,m,T). \tag{11}$$

*2.2 Image reconstruction*

The tomographic images of the fluorophore concentrations are obtained by solving the inverse problems [5] reconstructing $\mu_a(\mathbf{r}) + \varepsilon N(\mathbf{r})$ in Eq. (1) and $\mu_a(\mathbf{r})$ in Eq. (6) from the input data of the featured data extracted from the temporal profiles of the excitation and fluorescence light measured by a time-resolved measurement system. Figure 1 shows the concept of the process of image reconstruction in this study. Firstly, the powers of the excitation and fluorescence lights measured at the multiple positions at the object surface, $\Gamma_x(\mathbf{r}_b,t)$ and $\Gamma_m(\mathbf{r}_b,t)$, are obtained by time-resolved measurements. Secondly, a deconvolution process using the Wiener filtering [31] calculates the power of the zero-lifetime emission, $\Gamma^*_m(\mathbf{r}_b,t)$, by use of Eqs. (4) and (11) as well as the known lifetime, $\tau$. This deconvolution and noise suppression process is carried out for only the measured time-resolved data and the process is done prior to iteration for reconstruction taking only a few second in our image reconstruction process. If the total light approach is not used the convolution of Eq. (4) for the forward calculation should be done for every FEM node and every iterative updating process. Therefore, the total light approach reduces the calculation load for reconstruction. Then the measured total light, $\Gamma_T(\mathbf{r}_b,t)$, is obtained using Eqs. (5) and (11). It is known that full use of the temporal profiles in the reconstruction process improves the quality of the reconstructed images at the cost of long computation time. Here we employ the mean times of flight of the excitation and total light defined by Eq. (12), $<t(\mathbf{r}_b)>_x$ and $<t(\mathbf{r}_b)>_T$, as the input data for image reconstruction as the previous paper which proposed the total light approach [21],

$$<t(\mathbf{r}_b)>_\nu = \frac{\int_0^\infty t\Gamma_\nu(\mathbf{r}_b,t)dt}{\int_0^\infty \Gamma_\nu(\mathbf{r}_b,t)dt}, \quad (\nu = x,T). \tag{12}$$

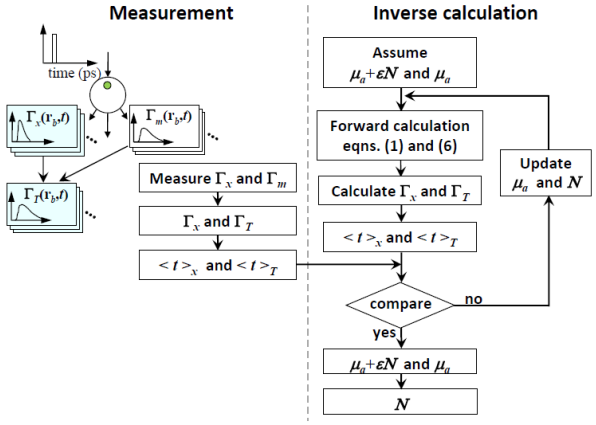


Fig. 1. Concept of fluorescence tomography. It consists of measurements of the excitation and fluorescence emission light and image reconstruction process by solving the inversion problem.

#178955 - $15.00 USD Received 31 Oct 2012; revised 12 Jan 2013; accepted 14 Feb 2013; published 28 Mar 2013

The inverse calculation is performed as the following. Firstly, the photon diffusion equations of light propagation are numerically solved with assuming the distributions of the optical properties, $\mu_{ax}(\mathbf{r})$ ( = $\mu_a(\mathbf{r})$ + $\varepsilon N(\mathbf{r})$) and $\mu_{aT}(\mathbf{r})$ ( = $\mu_a(\mathbf{r})$), using FEM. From the calculated powers of the excitation and total light, $\hat{\Gamma}_x(\mathbf{r}_b,t)$ and $\hat{\Gamma}_T(\mathbf{r}_b,t)$, the calculated mean times-of-flight, $<\hat{t}(\mathbf{r}_b)>_x$ and $<\hat{t}(\mathbf{r}_b)>_T$ are obtained. Although the diffusion coefficient, $D(\mathbf{r})$, varies with organs it is given homogeneously as 0.39 mm as a known value in this study by assuming that the differences in the scattering coefficients of biological tissues are not large. This assumption can be one of the causes of errors in the reconstructed images. Then the measured mean times-of-flight of the excitation and total light, $<t(\mathbf{r}_b)>_x$ and $<t(\mathbf{r}_b)>_T$, are compared with the calculated ones, $<\hat{t}(\mathbf{r}_b)>_x$ and $<\hat{t}(\mathbf{r}_b)>_T$, and the distributions of the optical properties, $\mu_{ax}(\mathbf{r})$ and $\mu_{aT}(\mathbf{r})$, are updated using Eq. (13),

$$\mathbf{M}_\nu - \mathbf{F}_\nu(\boldsymbol{\chi}_k) = \mathbf{J}_\nu(\boldsymbol{\chi}_k)\delta\boldsymbol{\chi}_k \quad (\nu = x,T), \tag{13}$$

where $\mathbf{M}_\nu$ and $\mathbf{F}_\nu(\boldsymbol{\chi}_k)$ are vectors with their elements consisting of $<t(\mathbf{r}_b)>_\nu$ and $<\hat{t}(\mathbf{r}_b)>_\nu$, respectively, $\boldsymbol{\chi}_k$ is a vector with its elements consisting of $\mu_{ax}(\mathbf{r})$ and $\mu_{aT}(\mathbf{r})$ of the finite element in FEM at the $k$-th iteration, $\delta\boldsymbol{\chi}_k$ is the update of $\boldsymbol{\chi}_k$, $\mathbf{J}_\nu(\boldsymbol{\chi}_k)$ is the Jacobian matrix which describes the changes in $<\hat{t}(\mathbf{r}_b)>_\nu$ when $\mu_{a\nu}(\mathbf{r})$ of each finite element changes infinitesimally. The update $\delta\boldsymbol{\chi}_k$ is calculated with the algebraic reconstruction technique (ART) as Eq. (14),

$$\delta\boldsymbol{\chi}_k^{j+1} = \delta\boldsymbol{\chi}_k^{j} + \frac{\left[h^{(j)} - \mathbf{J}_\nu^{(j)}(\boldsymbol{\chi}_k)\cdot\delta\boldsymbol{\chi}_k^{j}\right]}{\left\|\mathbf{J}_\nu^{(j)}(\boldsymbol{\chi}_k)\right\|^2}\left[\mathbf{J}_\nu^{(j)}(\boldsymbol{\chi}_k)\right]^T, \ (\nu = x,T), \tag{14}$$

where the superscript, $j$, denotes the $j$-th measurement position with the maximum of the product of the source and detector numbers, $\mathbf{J}_\nu^{(j)}(\boldsymbol{\chi}_k)$ is the $j$-th row vector of the matrix $\mathbf{J}_\nu(\boldsymbol{\chi}_k)$, $h^{(j)}$ is the $j$-th element of the vector $\mathbf{M}_\nu - \mathbf{F}_\nu(\boldsymbol{\chi}_k)$.

The solutions of $\mu_{ax}(\mathbf{r})$ and $\mu_{aT}(\mathbf{r})$ are obtained when the iteration reaches convergence where the updates of $\mu_{ax}(\mathbf{r})$ and $\mu_{aT}(\mathbf{r})$ becomes less than a specified small number. From the solutions of $\mu_{ax}(\mathbf{r}) = \mu_a(\mathbf{r}) + \varepsilon N(\mathbf{r})$ and $\mu_{aT}(\mathbf{r}) = \mu_a(\mathbf{r})$, the tomographic image of $N(\mathbf{r}) = (\mu_{ax}(\mathbf{r}) - \mu_a(\mathbf{r}))/\varepsilon$ is finally obtained.

The advantage of the total light approach is to reduce the computational time for Eq. (4) as mentioned above. It takes a long computation time to calculate the convolution in each updating process in many iterations, while only one calculation of deconvolution prior to the iterative process is required by the total light approach. In this study, we use only the time-of-flight data for reconstruction. But the total light approach allows the users to use the entire time-resolved data with relatively small computation load. The reconstruction procedure presented in this paper is basically the double DOTs for the excitation and total lights. Any kind of the featured data used in several DOT schemes can be applied to reconstruct the fluorophore concentrations. Time-resolved profile is affected by the absorption coefficient. So the features of the time-resolved data reflect the absolute value of the optical properties. Therefore DOT can reconstruct the absorption coefficient by using the featured data. Mean time-of-flight data is not dependent on the intensity of the detected light. Hence the calibrations of source and detector are not so important. A possible disadvantage of the proposed method is that the method inherits low spatial resolution of DOT.

Reconstruction of the fluorophore concentrations only can be done with CW systems. Time-resolved systems are not necessarily needed for reconstruction only the fuorophore concentration. Therefore, the time-resolved measurement system employed in this study is over-specified for reconstruction of only the fluorophore concentration. The fluorescence lifetime can be reconstructed by better use of the measured time-resolved data. Simultaneous

#178955 - $15.00 USD Received 31 Oct 2012; revised 12 Jan 2013; accepted 14 Feb 2013; published 28 Mar 2013

reconstruction of the fluorescence yield (i.e., fluorophore concentration) and lifetime is possible [25], but the reconstruction of the lifetime will be more easily performed if the distribution of the fluorophore concentration is known as prior information. Now, the fluorophore concentration reconstructed first by the total light approach can provide prior information for reconstruction of the lifetime using Eq. (2). This process may be another advantage of the total light approach applied to time-domain FDOT.

## 3. Experimental setup and objects

### *3.1 Fluorescence characteristics of fluorophore*

Indocyanine green (ICG, Sigma-Aldrich) was employed as the fluorophore in this study. ICG is approved for injection to humans and widely used clinically for investigating hepatic function and retinal angiography, etc. It has absorption and emission spectra in the near-infrared wavelength range where light is more transparent to biological tissues. This property is very important for fluorescence tomography to be applied to *in vivo* animals. Figure 2 shows the measured absorption and emission spectra of ICG contained in 0.8% Intralipid solution which has scattering characteristics similar to biological tissues. The peak wavelengths of absorption and emission are 767 nm and 820 nm, respectively. The specific extinction coefficient, fluorescence lifetime and quantum yield around the wavelength of 800 nm are given as $\varepsilon = 0.04\ \mathrm{mm^{-1}/\mu M}$, $\tau = 0.47$ ns, $\gamma = 0.03$ from the literatures [32–34].

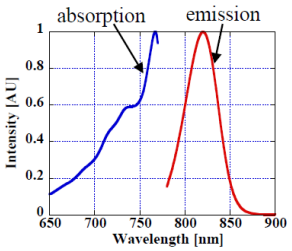


Fig. 2. Absorption and emission spectra of ICG mixed in Intralipid.

### *3.2 Time-resolved measurement system*

Figure 3 shows the schematics of the picosecond time-resolved measurement system used in this study. It had a light source of a diode laser emitting ultrashort pulse light with a wavelength of 759 nm, a pulse width of about 100 ps, a repetition rate of 5 MHz and an average power of 0.25 mW. The temporal profiles were measured by a time-correlated single photon counting (TCSPC) system which had a time-resolution of about 100 ps. Please refer to a literature for the details [35]. Multiple source and detector fiber bundles were used for phantom and mouse experiments, respectively. 12 source and detector bundles were alternatively attached onto the surface of the cylindrical phantom in the plane perpendicular to the cylinder axis with an equal spacing. For *in vivo* mouse experiments, 8 source and detector fiber bundles were attached to the surface of a mouse holder as well. The outer diameters of both the source and detector fiber bundles were 4.0 mm.

The ultrashort pulse light from the light source was introduced into one source fiber bundle, and the lights collected by the detector fiber bundles were led to the TCSPC system one by one through a switching device. By switching the source fiber bundle one by one, 12 × 12 (phantom experiments) or 8 × 8 (mouse experiments) temporal profiles were acquired for each of excitation and emission lights. When measuring emission light a long pass filter (IR82, Fuji film) was used to cut excitation light and a total of 12 × 12 × 2 or 8 × 8 × 2 temporal profiles were obtained for one image. Figure 4 shows the transmission spectrum of the filter as well as the excitation wavelength and the wavelength range of emission light. The transmittance of the single long pass filter at the excitation wavelength was 2%. We used three long pass filters in series and obtained 0.0008% transmittance at the excitation

#178955 - $15.00 USD Received 31 Oct 2012; revised 12 Jan 2013; accepted 14 Feb 2013; published 28 Mar 2013

wavelength. The measured temporal profiles were the results of convolution between the temporal response for the ideal impulse light source and the instrument function including the finite pulse width of the light source and the time-resolution of the TCSPC system. Because the forward calculation assumes the ideal impulse source the mean time-of-flight data for the ideal impulse source were obtained using the following simple Eq. (15) [25,36],

$$< t >=< t >_m - < t >_{IRF}, \tag{15}$$

where $<t>_m$ is the measured mean time-of-flight and $<t>_{IRF}$ is that of the instrumental function.

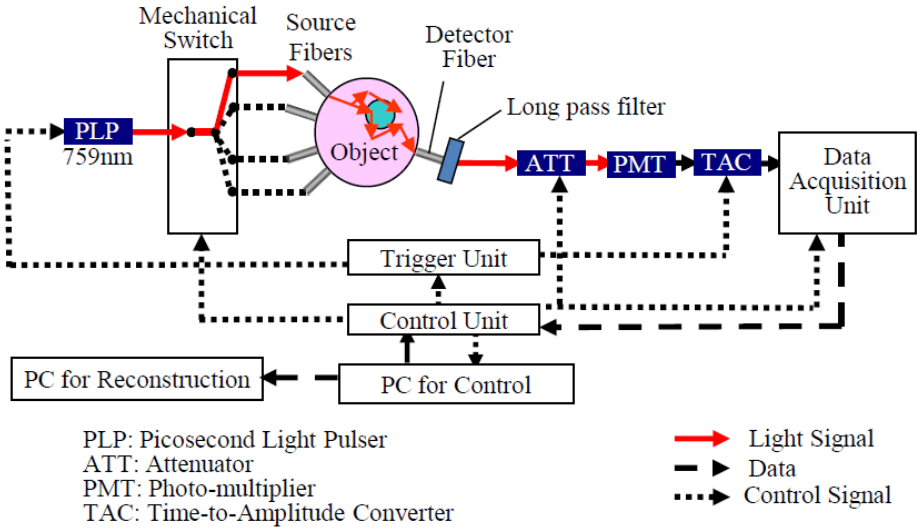


Fig. 3. Schematics of the picosecond time-resolved measurement system [35]. Long pass filter for measurement of emission light was removed for measurement of excitation light. Arrangement of the long pass filter in this figure was for mouse experiment. For phantom experiment the long pass filter was attached on the phantom surface.

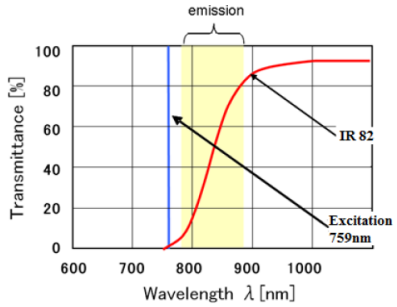


Fig. 4. The transmission spectrum of the long pass filter IR-82 as well as the excitation wavelength and the wavelength range of emission light.

### *3.3 Phantom experiments*

Figure 5 shows a typical cylindrical phantom used in this study. The phantoms were made of polyacetal resin which had the scattering characteristics similar to biological tissues. The reduced scattering and absorption coefficients of polyacetal resin at the wavelength of 800 nm were $\mu_s' = 0.863$ mm$^{-1}$ and $\mu_a = 0.0006$ mm$^{-1}$, respectively. The diameter and height of the phantoms were 30 mm and 85 mm, respectively, and the phantoms had one or two cylindrical target holes with a height of 65 mm and a diameter of 4 mm, 5 mm or 6 mm where 0.8% Intralipid solutions containing 0.25 μM to 2.0 μM ICG were injected. The 0.8% Intralipid

#178955 - $15.00 USD Received 31 Oct 2012; revised 12 Jan 2013; accepted 14 Feb 2013; published 28 Mar 2013

solutions had the scattering characteristics similar to polyacetal resin. Table 1 summarizes the conditions of 10 phantoms used in the phantom experiments, where the origin of the *x*-*y* coordinate was at the cylinder axis.

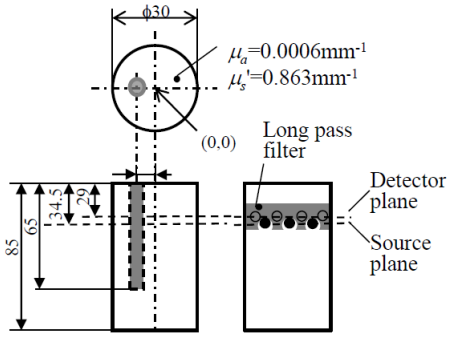


Fig. 5. Schematics of the phantoms. The long pass filter was attached on the phantom surface, and its position was shifted according to the measurement of the excitation or emission light. The long pass filters were placed on the detector plane only when measuring the emission light.

**Table 1. Summary of 10 phantoms used in the experiments**

| Phantom No. | Number of targets | Diameter of target [mm] | Position of target center ($x$, $y$) [mm] | ICG in target [μM] |
|---|---|---|---|---|
| 1 | 1 | 4.0 | (−7.5, 0) | 1.0 |
| 2 | 1 | 5.0 | (−7.5, 0) | 1.0 |
| 3 | 1 | 6.0 | (−7.5, 0) | 1.0 |
| 4 | 1 | 6.0 | (−7.5, 0) | 2.0 |
| 5 | 1 | 6.0 | (−7.5, 0) | 0.50 |
| 6 | 1 | 6.0 | (−7.5, 0) | 0.25 |
| 7 | 1 | 6.0 | (−11.5, 0) | 1.0 |
| 8 | 2 | 6.0 | (−6.0, 0), (6.0, 0) | 1.0, 1.0 |
| 9 | 2 | 6.0 | (−5.0, 0), (5.0, 0) | 1.0, 1.0 |
| 10 | 2 | 6.0 | (−4.0, 0), (4.0, 0) | 1.0, 1.0 |

Twelve fiber bundles were used for both the source and detector and the plane of the detector fiber bundles was 5.5 mm below that of the source fiber bundles because of the geometrical limitation. When measuring the emission light the long pass filter stated above was put on the phantom surface as shown in Fig. 5.

The image reconstruction was carried out with the homogeneous background reduced scattering coefficient, $\mu_s' = 0.863$ mm$^{-1}$, which was held constant during the inversion process. It started with the initial guess of the homogeneous absorption coefficient, $\mu_a = 0.0006$ mm$^{-1}$. The update was iterated until the reconstructed values $\boldsymbol{\chi}_k$ was found to converge by checking that the norm of $\delta\boldsymbol{\chi}_k$ was sufficiently small.

*3.4 In vivo mouse experiment*

Figure 6 shows the schematics of an *in vivo* mouse experiment. In order to measure the weak fluorescence light it was necessary to keep good contact between the fiber bundles and the mouse skin. But, the mouse skin was very soft and it was difficult to keep good contact during the whole experimental period. In addition it was very difficult to attach a total of 16 fiber bundles in one plane around the deformable mouse abdomen with a diameter less than 30 mm. Then, an anesthetized mouse was fixed rightly in a mouse holder of an annular black polyacetal cylinder with inner and outer diameters of 23 mm and 30 mm, respectively, and with a length of 40 mm. A total of 16 fiber bundles were attached onto the surface of the mouse holder with an equal spacing of 22.5° in one plane perpendicular to the cylinder axis as shown in Fig. 7(a). In the image reconstruction process, the whole volume consisting of the mouse and mouse holder was the object for fluorescence tomography. To avoid light

#178955 - $15.00 USD Received 31 Oct 2012; revised 12 Jan 2013; accepted 14 Feb 2013; published 28 Mar 2013

propagation along the surface of the mouse holder due to bad contact between the fiber bundles and the mouse holder, a black soft rubber covered the whole surface of the mouse holder except the positions of the fiber bundles.

The fluorophore target was a capsule containing 1 μM ICG mixed in a 0.8% Intralipid solution. The plexiglass capsule had inner and outer diameters of 4 mm and 6 mm, respectively, and a length of 30 mm as shown in Fig. 7(b). We intended to simulate a grown tumor accumulating a fluorophore by using the ICG capsule. The experiment was carefully carried out to place the capsule rightly at the position as illustrated in Figs. 6 and 7, but the positional error might have occurred during the preparation. We ignored the influence of the plexiglass because it was thin and strong diffusion effect by the tissues must overwhelm the influence, but there is a possibility that the light propagation was slightly influenced by the non-scattering and non-absorbing plexiglass resulting in slightly stronger emission light and higher fluorophore concentration of the reconstructed target. A long pass filter to cut the excitation light when measuring fluorescence light was installed in a switching device of the detector fiber.

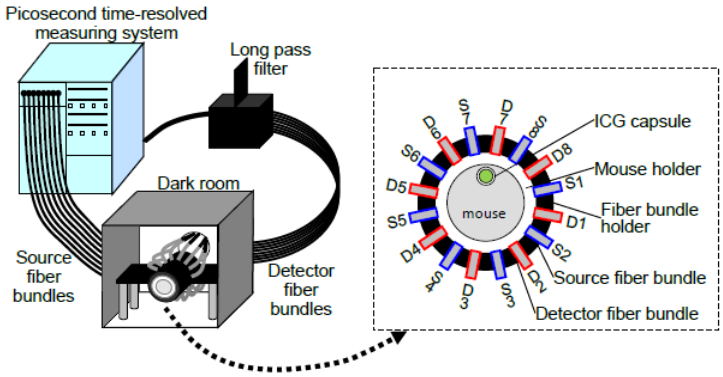


Fig. 6. Experimental setup for mouse experiments.

The mouse experiment was conducted with the approval of the committee of Tokyo Metropolitan Institute of Medical Science and in accordance with the institute guidelines for animal experiments. A mouse (Jc1:ICR, 17 week old, 43.0 g) was weakly anesthetized by breathing diethyl ether first, and deeply anesthetized by injecting pentobarbital into the abdomen. The hair around the abdomen was removed by a hair removing cream. The fluorophore capsule was implanted beneath the skin with its center located at the position of $(x, y, z) = (0, 8, 0)$ when the center of the whole object was the coordinate origin, $(x, y, z) = (0, 0, 0)$. The whole object including the mouse and mouse holder attached with the fiber bundles was fixed in a dark room to avoid stray light and time-resolved measurement was performed. The accumulation time for measuring one temporal profile was 15 sec, and it took about 45 min to acquire a set of the temporal profiles necessary for reconstructing one image, because only one PMT was used for detection and the 16 detector fibers were switched manually. By some modification of the system for simultaneous use of 16 PMTs, it is possible to reduce the acquisition time to a few minutes which are short enough for practical use.

As in the case of the phantom experiments, the image reconstruction was carried out with the homogeneous background reduced scattering coefficient, $\mu_s' = 0.863$ mm$^{-1}$, which was held constant during the inversion process. It started with the initial guesses of $\mu_a = 0.003$ mm$^{-1}$ and 0.0006 mm$^{-1}$ for the mouse and mouse holder, respectively.

One updating process took about 4 seconds, and the updating process was terminated when the difference in the residual errors between two successive iterations was smaller than 0.003% of the initial residual error.

#178955 - $15.00 USD Received 31 Oct 2012; revised 12 Jan 2013; accepted 14 Feb 2013; published 28 Mar 2013

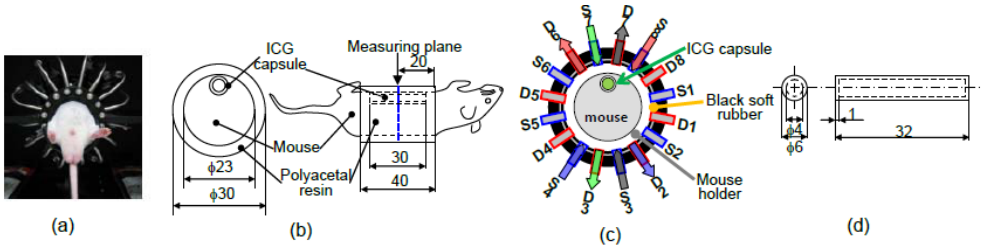


Fig. 7. (a) Picture of an anesthetized mouse fixed in a mouse holder, (b) size of the mouse holder and position of the ICG capsule embedded in the mouse abdomen with the measurement plane indicated by a vertical line, (c) arrangement of the source and detector fiber bundles; 8 source fiber bundles (S1 to S8) and 8 detector fiber bundles (D1 to D8) were alternatively attached onto the surface of the mouse holder with an equal spacing, (d) size of the ICG capsule containing 1 μM ICG mixed in a Intralipid solution.

## 4. Experimental results and discussions

### *4.1 Phantom experiments*

#### 4.1.1 Measured temporal profiles

Figure 8 shows the measured temporal profiles of the excitation and fluorescence emission, $\Gamma_x(\mathbf{r}_b,t)$ and $\Gamma_m(\mathbf{r}_b,t)$, as well as those of the total light and zero-lifetime emission, $\Gamma_T(\mathbf{r}_b,t)$ and $\Gamma^*_m(\mathbf{r}_b,t)$, for the case of phantom No. 3. Figures 8(a) and 8(b) are the cases of short and long distances between the source and detector positions, respectively. The measured excitation light, $\Gamma_x(\mathbf{r}_b,t)$, in Fig. 8(b) varies more slowly and its peak shifts to later time than that in Fig. 8(a) because it is more strongly affected by scattering. A similar behavior is observed for the measured temporal profiles of fluorescence emission, but the values of the fluorescence emission are about one-order of magnitude smaller than those of the excitation. The temporal profiles of $\Gamma^*_m(\mathbf{r}_b,t)$ are accompanied with noises due to the deconvolution process which enhanced noises, but the noise levels were acceptable for image reconstruction.

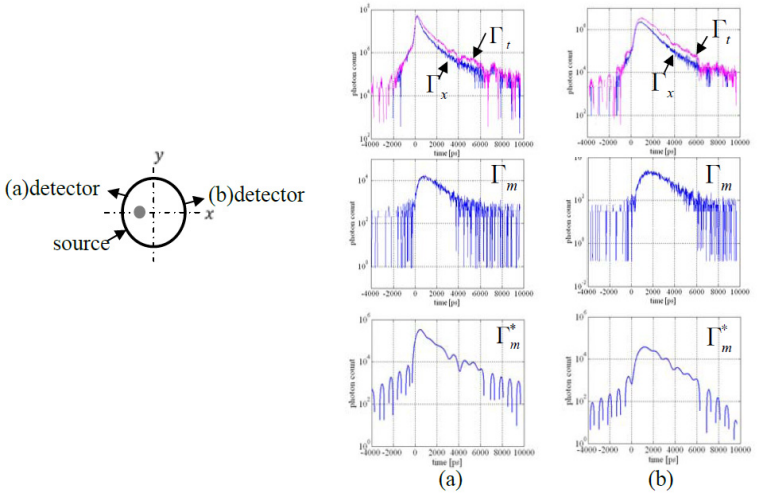


Fig. 8. Measured temporal profiles of the excitation and emission light, $\Gamma_x(\mathbf{r}_b,t)$ and $\Gamma_m(\mathbf{r}_b,t)$, respectively, together with the calculated zero-lifetime emission and total light, $\Gamma^*_m(\mathbf{r}_b,t)$ and $\Gamma_T(\mathbf{r}_b,t)$, respectively, for the case of phantom No. 3. (a) and (b) are for the cases of the detectors close to and far from the source, respectively.

In our previous report [21], we investigated the effect of the noise. The noise gave no effect on the reconstructed images for S/N ratio smaller than 40 dB. When S/N ratio was 25

#178955 - $15.00 USD Received 31 Oct 2012; revised 12 Jan 2013; accepted 14 Feb 2013; published 28 Mar 2013

dB, the target was reconstructed, although the absorption coefficient was reconstructed less than 40% of the true value.

4.1.2 Results of image reconstruction

Figure 9 shows the reconstructed images of fluorophore concentrations in [μM] for 10 phantoms in Table 1. The color bars are normalized by the original concentration, and the graphs show the concentration profiles along the $x$ axis with the red lines showing the true profiles.

Figures 9(a) to 9(c) compare the effect of the target size. Although the positions of the target can be identified correctly the reconstructed peak concentrations increase with the target size, i.e., the peak concentration for phantom No. 1 with a target diameter of 4 mm is about 25% of the true value while that for phantom No. 3 with a target diameter of 6 mm is about 60% of the true value. This trend is consistent with the results of simulation in the previous report [21].

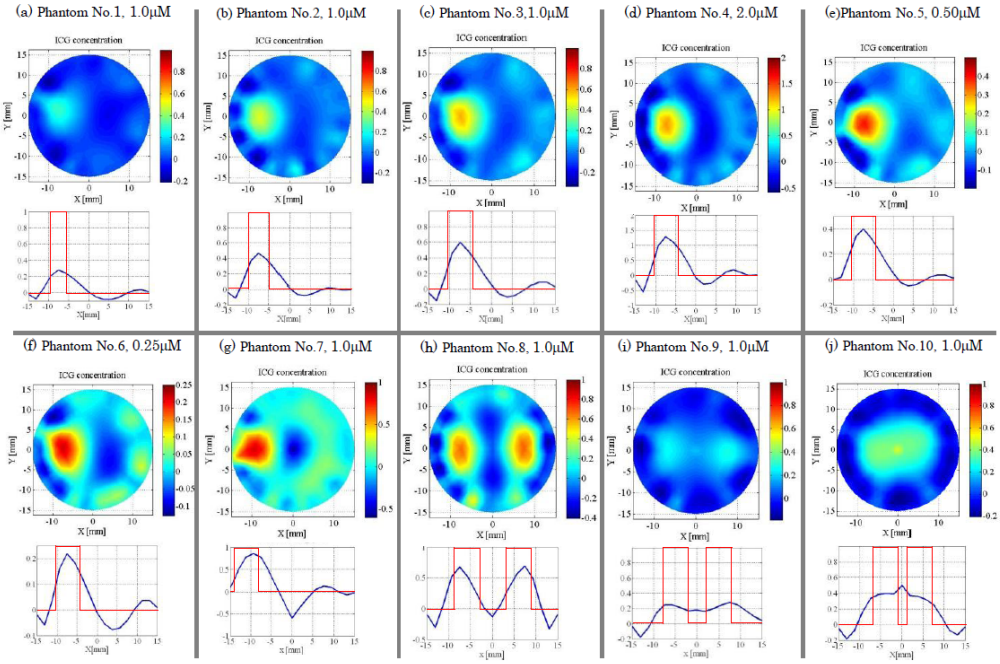


Fig. 9. The reconstructed images of ICG concentration for the ten phantoms listed in Table 1. The unit of the color bars is [μM].

Figures 9(c), 9(d), 9(e) and 9(f) shows the results for phantoms No. 3, 4, 5 and 6, respectively, illustrating the effect of the target concentration with the fixed size and position of the targets. The position of the target was correctly identified in each case. The reconstructed peak concentrations are about 60% of the true values for phantoms No. 3 (true: 1.0 μM) and No. 4 (true: 2.0 μM) and about 80% for phantoms No. 5 (true: 0.5 μM) and No. 6 (true: 0.25 μM). These results indicate that the reconstructed peak concentration depends on the true concentration, but the previous simulation results did not show the dependency [21]. This disagreement between the phantom experiments and simulation results may be caused by a wrong estimation of the specific extinction coefficient, $\varepsilon$. The concentrations are calculated by dividing the subtraction between $\mu_a(\mathbf{r}) + \varepsilon N(\mathbf{r})$ and $\mu_a(\mathbf{r})$ by $\varepsilon$. In this study $\varepsilon$ was given constant $\varepsilon = 0.04$ mm$^{-1}$μM$^{-1}$ for all the cases according to the literature [32] which also reported the dependency of $\varepsilon$ on the ICG concentration over 1 μM due to self-absorption. It will be necessary to correctly measure not only $\varepsilon$, but also other fluorescence characteristics of lifetime, $\tau$, and quantum yield, $\gamma$, which are important constants to calculate the total light $\Phi_t$

#178955 - $15.00 USD Received 31 Oct 2012; revised 12 Jan 2013; accepted 14 Feb 2013; published 28 Mar 2013

from Eqs. (4) and (5), toward more precise validation of the total light approach for fluorescence tomography.

Figure 9(g) shows the image for phantom No. 7 in which the position of the target was 4.0 mm closer to the surface than phantom No. 3. The reconstructed peak concentration is about 90% of the true value, which is better than that for phantom No. 3. But, an artifact with a negative concentration appeared in the central area of the image. Generally speaking, fluctuations in the reconstructed distributions are often observed in images reconstructed by inversion processes, and it will be necessary to employ some regularization method to suppress the fluctuation and artifacts [37]. Another reason of the artifacts may be the employment of the photon diffusion equation which is the approximation of the radiative transfer equation. The photon diffusion approximation is valid for the area and time where photons have propagated more than a few millimeters. Therefore, when the target exists very close to the surface the photon diffusion equation may not be an appropriate propagation model [27].

Figures 9(h), 9(i) and 9(j) show the reconstructed images for phantoms No. 8, 9 and 10 having two targets with different center-to-center separation (CCS) of 12 mm, 10 mm and 8 mm, respectively, but the same size and ICG concentration. The two targets are clearly separated and the reconstructed peak concentration was about 60% of the true value in the image of phantom No. 8 shown in Fig. 9(h) while the two targets were not clearly separated in Figs. 9(i) and 9(j) with the CCS of 10 mm and 8 mm, respectively. In the previous simulation [21] two targets were clearly separated even when the CCS was as small as 6 mm although not shown in this paper. The degraded spatial resolution in the experiment must be due to larger noises in the measured temporal profiles than those assumed in the simulation. The spatial resolution may be improved by employing a regularization method [37] as well as the variable regularization parameter depending on the depth from the surface [38].

### *4.2 In vivo mouse experiment*

#### 4.2.1 Measured temporal profiles

The arrangement of the source and detector fiber bundles is shown in Fig. 10(a) where eight sources and detectors, S1 to S8 and D1 to D8, respectively, were attached onto the outer surface in the central plane of the mouse holder alternatively with an equal spacing. The temporal profiles of the measured powers of the excitation and fluorescence emission light as well as those of the zero-lifetime emission and total light are shown in Fig. 10(b) to Fig. 11(e). The ordinates are the photon counts measured by the TCSPC system, and only Fig. 10(c) for fluorescence emission is in a linear scale because the photon counts were much smaller than other light which are in logarithmic scales. Each figure shows the cases where (i) both the source and detector were close to the target (S8-D6), (ii) the source was close to the target while the detector was far from the target (S7-D3) and vice versa (S3-D7), and (iii) both the source and detector were far from the target (S4-D2). When the source or detector was far from the target the magnitudes of the fluorescence emission were in the same order of noises. Resultantly, the noises of the zero-lifetime emission and total light were observed larger than those of the excitation light. Note that the temporal profiles of the zero-lifetime emission and total light were smoothed due to Wiener filtering. The integration period of time for calculating the mean time-of-flight of the excitation light, $<t_x>$, in Eq. (12) was determined to be from the time origin to the time when the temporal curve decreased to the noise level after the peak. The same integration period of time was used for calculating the mean time of flight of the total light, $<t_T>$.

When looking at the temporal profiles of fluorescence emission, Fig. 10(c), the magnitude of the profile for the case of (ii) (S7-D3 and S3-D7, the source was close to the target while the detector was far from the target and vice versa) was almost the order of noises. Then, for the case of (iii) (S4-D2, both the source and detector were far from the target) the fluorescence emission from ICG would not be observed. But, the fluorescence emission of the case (iii) was stronger than that of the case (ii). The emission of the case (iii) must be autofluorescence

#178955 - $15.00 USD Received 31 Oct 2012; revised 12 Jan 2013; accepted 14 Feb 2013; published 28 Mar 2013

from the mouse tissues. This conjecture is proved by the fact that very similar strong emissions were observed for other combinations of the source and detector with the same distance as that of S4-D2, i.e., other combinations are S1-D2, S2-D3, S3-D4, S4-D5, S2-D8, S3-D1, S5-D3, S6-D4. There was a possibility that the light intensity observed by the combination of S4-D2 was a leakage of the excitation light. But that light was not eliminated by increasing the attenuation of the optical filter at the excitation wavelength. This fact indicated that the wavelength of the light was different from that of the excitation light. So the light observed by S4-D2 must be autofluorescence. Image reconstruction was performed with the emission data including autofluorescence.

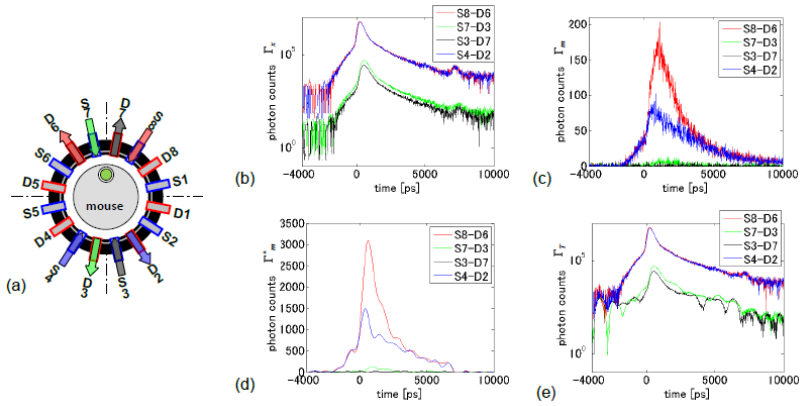


Fig. 10. (a) The arrangement of the source and detector fiber bundles, and the measured temporal profiles of (b) the excitation, (c) fluorescence emission, (d) zero lifetime emission and (e) total light.

### 4.2.2 Reconstructed image

The reconstructed ICG concentration distribution is shown in Fig. 11 where large and small white circles indicate the interface between the mouse and mouse holder and the true position of the ICG capsule, respectively. In the reconstruction process, the absorption coefficient of the mouse holder was fixed as that of polyacetal resin, and the ICG concentration within the mouse holder was fixed as zero. An area with high ICG concentration was reconstructed almost right on the true position of the ICG capsule with the maximum concentration of 0.94 μM, the area occupying the concentration higher than the half maximum of about 1.6 times the true area, the integrated ICG concentration over this area of about 1.2 times the true value, and the position shift of the maximum concentration of 2.5 mm from the true position.

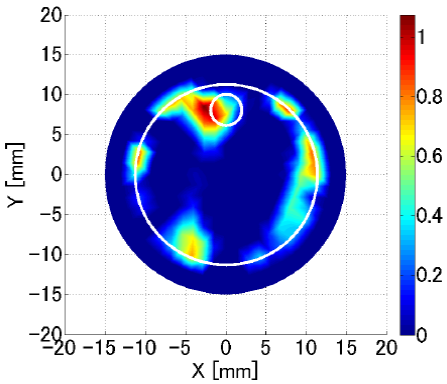


Fig. 11. Reconstructed image of ICG concentration for mouse experiment. The unit of the color bar is [μM].

#178955 - $15.00 USD Received 31 Oct 2012; revised 12 Jan 2013; accepted 14 Feb 2013; published 28 Mar 2013

Artifacts with the maximum concentration of 0.91 μM appeared along the interface between the mouse and mouse holder. It is known that much of the autofluorescence in animals is mainly emitted from the skin and colon [39]. Therefore, the major reason of the artifacts in Fig. 11 must be autofluorescence from the mouse skin because the colon in the mouse was out of the measuring plane. Other possible reasons of the artifacts are irregular contact between the fiber bundles and outer surface of the mouse holder and possible small gaps between the mouse skin and inner surface of the mouse holder. These irregular contacts will bring irregular light propagation which lead to deformation of the temporal profiles and to artifacts. In the mouse experiment these irregular contacts were eliminated as much as we could by careful setup of the experimental. Although artifacts appeared in the vicinity at the interface between the mouse and mouse holder, the ICG target was reconstructed reasonably well as in the phantom experiments.

In the phantom experiments, we employed polyacetal resin for the background phantom material which has very small absorption, $\mu_a = 0.0006$ mm$^{-1}$, while the additional absorption by ICG was $\varepsilon N = 0.01$ mm$^{-1}$ with $\varepsilon = 0.004$ mm$^{-1}$μM$^{-1}$ and $N = 0.25$ μM. Therefore, the contrast, i.e., the ratio of the absorption coefficient of the target to that of the background, was as large as 16.7 which may be easy to be reconstructed. But *in vivo* experiments using small animals, the background absorption coefficient is much larger in the order of 0.001 mm$^{-1}$ which leads to low contrast targets. Larger absorption by the background tissues in the mouse experiment than in the phantom experiments seems to degrade the quality of the reconstructed images, because the S/N ratio of the measured data was lowered. The reconstructed target, however, was well localized and had the ICG concentration higher than the true value in contrast to the results of phantom experiment. This can be another effect of the background with strong absorption. When the background has a large absorption coefficient, the light propagation path from the source to the detector becomes narrower. Narrower path makes it easy to identify the position of the target. As a result, the position and area of the target can be localized well. And it has been shown in the literature [37] that when the reconstructed target is well-localized, the absorption coefficient becomes larger. Another reason of the reconstructed ICG concentration higher than the true value may be the existence of the plexiglass capsule as stated above.

On the other hand, the small quantum yield of ICG in Intralipid ($\gamma = 0.03$) may become larger when ICG is combined with protein in blood, for example with high density lipoprotein [33]. This will make the fluorescence light stronger and the image reconstruction easy in small animals even with highly absorbing background. New fluorophores with high quantum yields in the near-infrared wavelength range are actively being developed for experiments using small animals. Employment of new fluorophores will improve the performances of fluorescence tomography in general.

## 5. Conclusions

Experiments using phantoms and mouse with the embedded ICG targets were conducted to demonstrate the total light approach for time-domain fluorescence tomography, and the followings were concluded.

The temporal profiles of the zero-lifetime emission and total light were obtained from the measured temporal profiles of the excitation and fluorescence emission light with removing the effect of the instrument function. The tomographic images of the ICG concentration were obtained from the measured mean time-of-flight data of the excitation and total light. In the reconstructed images of the phantom experiments, the positions, sizes and ICG concentrations of the embedded targets were reconstructed with the qualities similar to those in the previous simulation although the spatial resolution was worse than that of the previous simulation. In the reconstructed image of *in vivo* mouse experiments, the ICG target was again reconstructed reasonably well. However, the autofluorescence from the mouse body produced the artifacts in the vicinity of the mouse skin, and it is suggested that small gap between the mouse and inner surface of the mouse holder may lead to artifacts.

#178955 - $15.00 USD Received 31 Oct 2012; revised 12 Jan 2013; accepted 14 Feb 2013; published 28 Mar 2013

The total light approach for time domain FDOT was experimentally demonstrated, and further studies are expected for reconstruction of multiple fluorescence characteristics with full use of time domain data.

**Acknowledgments**

This work was partly supported by KAKENHI No. 19360098 of the Japanese government. F. Gao also acknowledges the funding supports from the National Natural Science Foundation of China (No. 30970775).

#178955 - $15.00 USD Received 31 Oct 2012; revised 12 Jan 2013; accepted 14 Feb 2013; published 28 Mar 2013